Supporting Information for

Asymmetric Contact Induced Self-Powered 2D In_2S_3 Photodetector towards High-Sensitivity and Fast-Response

Jianting Lu[1], Zhaoqiang Zheng[1, 2*], Jiandong Yao[3], Wei Gao[1], Ye Xiao[1], Menglong Zhang[4], Jingbo Li[1, 4, 5*]

[1] School of Materials and Energy, Guangdong University of Technology, Guangzhou, 510006, Guangdong, P. R. China.

[2] Department of Electronic Engineering, The Chinese University of Hong Kong, Hong Kong SAR, P. R. China.

[3] State Key Laboratory of Optoelectronic Materials and Technologies, Nanotechnology Research Center, School of Materials Science & Engineering, Sun Yat-sen University, Guangzhou, 510275, Guangdong, P. R. China.

[4] Institute of Semiconductors, South China Normal University, Guangzhou, 510631, P.R. China.

[5] State Key Laboratory for Superlattices and Microstructures, Institute of Semiconductors, Chinese Academy of Sciences, Beijing, 100083, P. R. China.

*Corresponding authors: zhengzhq5@mail2.sysu.edu.cn and jbli@semi.ac.cn

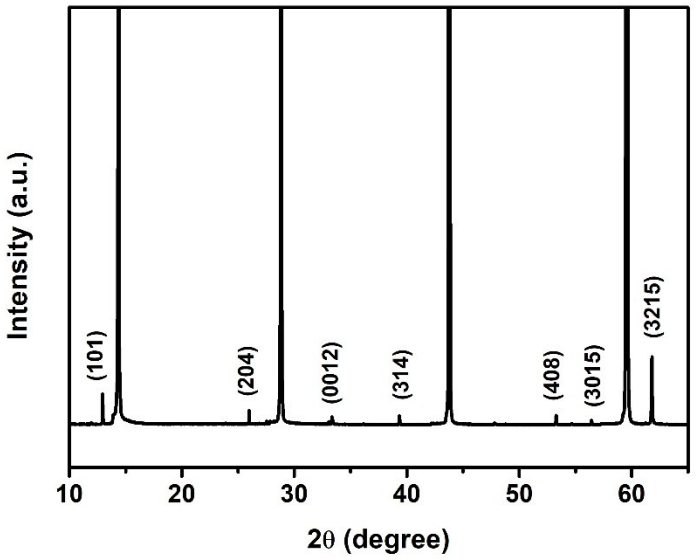

Figure S1. Enlarged XRD pattern of the prepared sample. The weak peaks can be indexed to tetragonal In_2S_3 (JCPDS 73-1366)[1, 2]. Actually, the tetragonal (JCPDS 73-1366) and cubic (JCPDS 51-1159) phases are only different in the arrangement of vacancies on tetrahedral cation sites, so that they share very similar crystal structure. During the preparation of In_2S_3 samples, environmental disturbances (especially the heating and cooling processes) will affect the defect distribution, resulting in samples with slightly different structures. However, as shown in the XRD pattern, the peak intensity of cubic In_2S_3 is much larger than that of tetragonal In_2S_3, indicating that the content of tetragonal In_2S_3 is very small and can be ignored.

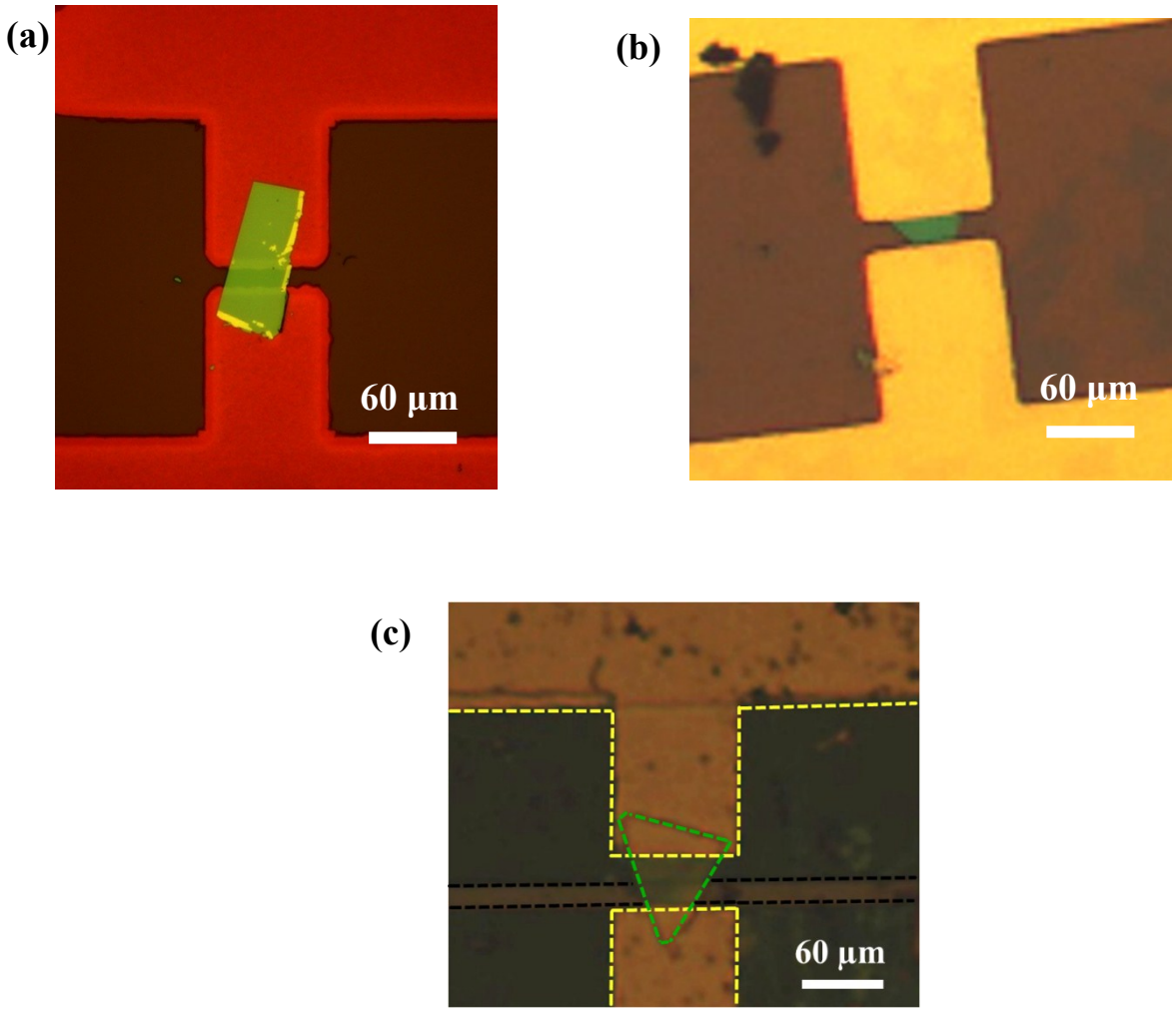

Figure S2. Optical images of the In_2S_3-based photodetectors with (a) symmetric contact lengths; (b) asymmetric contact lengths. (c) Optical image of the AC-In_2S_3/Si device.

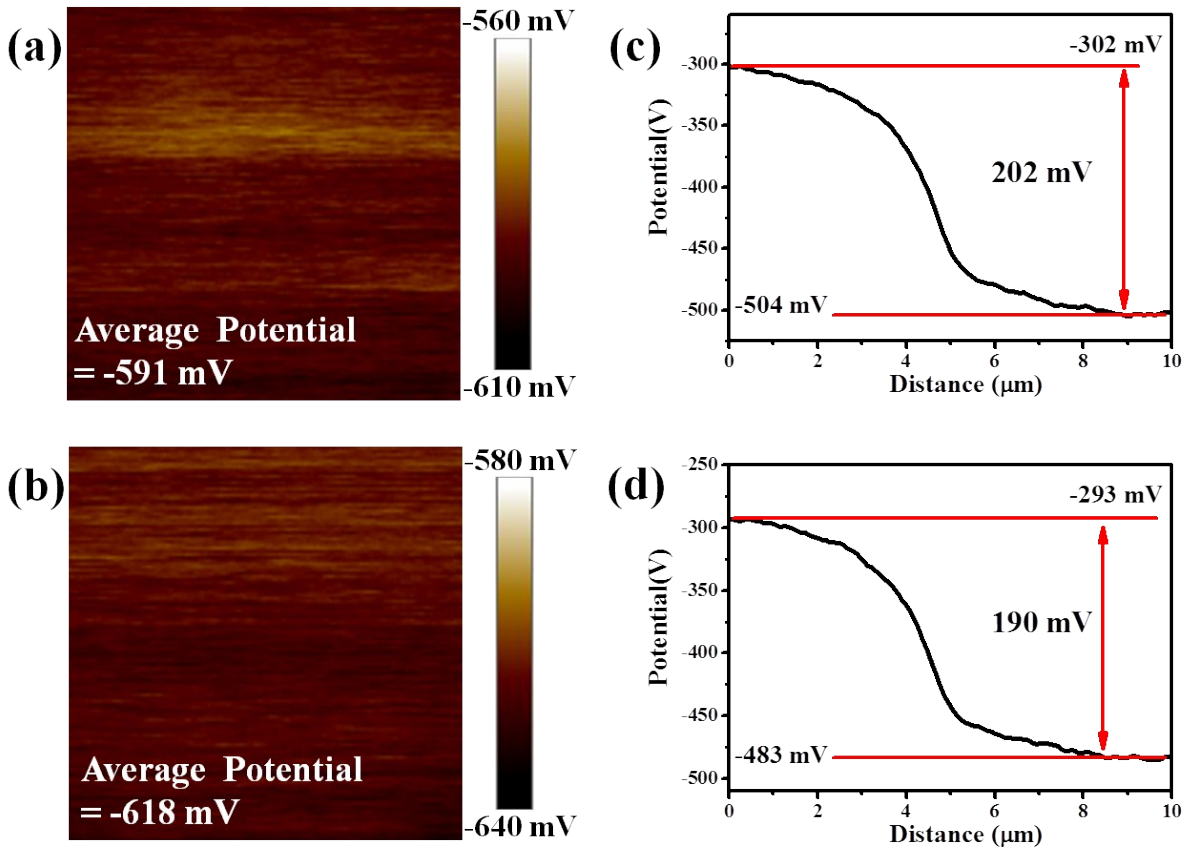

Figure S3. (a) SPD map of Au in dark. (b) SPD map of Au under white light illumination. (c) The calibrated SPD along the heterointerface of In_2S_3 and Si in dark. (d) The calibrated SPD along the heterointerface of In_2S_3 and Si under white light illumination.

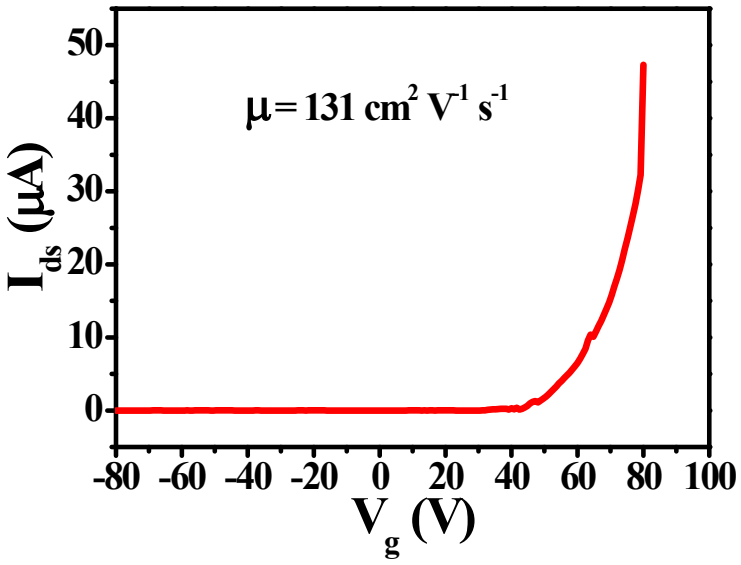

Figure S4. The transfer curve of planar In_2S_3 device. This device was fabricated as follows: The grown In_2S_3 nanoflake was firstly transferred onto the commercially purchased SiO_2 (300nm)/Si substrate. Then, planar Ti/Au (10/100 nm) electrodes were deposited via a stand photolithography process, followed by electron beam evaporation and and lift-off process.

The electron mobility can be acquired by the following equation[3, 4]

$$\mu = \frac{\partial I_{ds}}{\partial V_g}\left(\frac{Ld}{W\varepsilon_o\varepsilon_r V_{ds}}\right)$$

where L and W are the length and width of the channel, $\frac{\partial I_{ds}}{\partial V_g}$ is slope of the transfer curve, μ is mobility, ε_r is the relative static permittivity, ε_0 is the electric constant, and d is the thickness of the SiO_2 layer. Herein, V_{ds} = 2 V, L = 3 μm, W = 15 μm, d = 300 nm, $\varepsilon_0 = 8.85 \times 10^{-12}$ F/m and ε_r = 3.9. Based on the data shown in Figure S2, $\frac{\partial I_{ds}}{\partial V_g}$ = 1.51 $\times 10^{-5}$ A/V. Then, the electron mobility is calculated to be 131 $cm^2\ V^{-1}\ s^{-1}$.

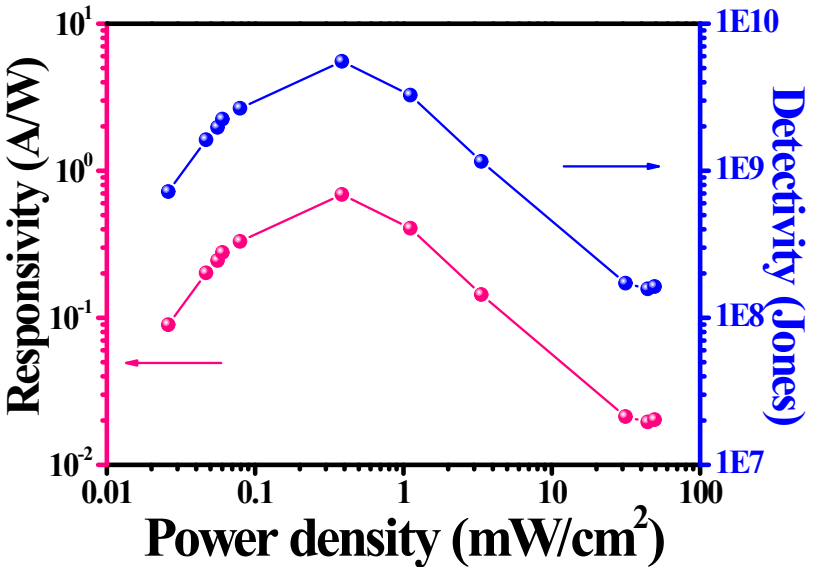

Figure S5. Photoresponsivity and detectivity as a function of incident light intensity of an AC-In_2S_3 device.

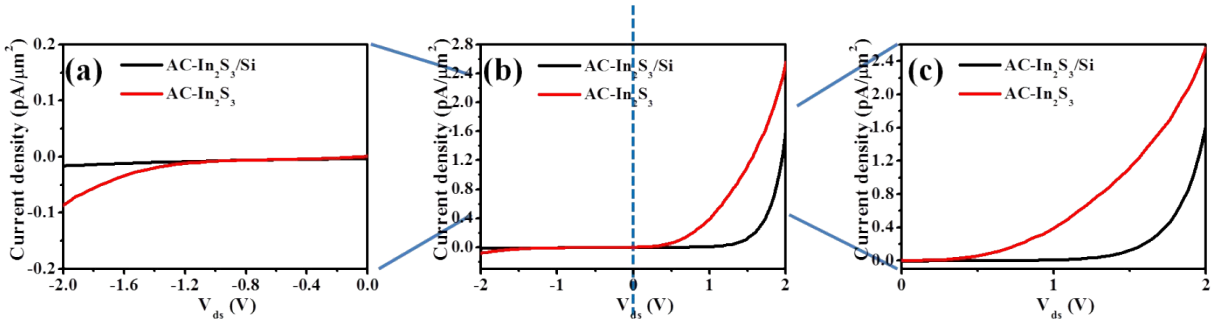

Figure S6. (a) The corresponding I–V curves of AC-In_2S_3 device and AC-In_2S_3/Si device in dark under negative bias. (b) The I–V curves of AC-In_2S_3 device and AC-In_2S_3/Si device in dark. (c) The corresponding I–V curves of AC-In_2S_3 device and AC-In_2S_3/Si device in dark under positive bias.

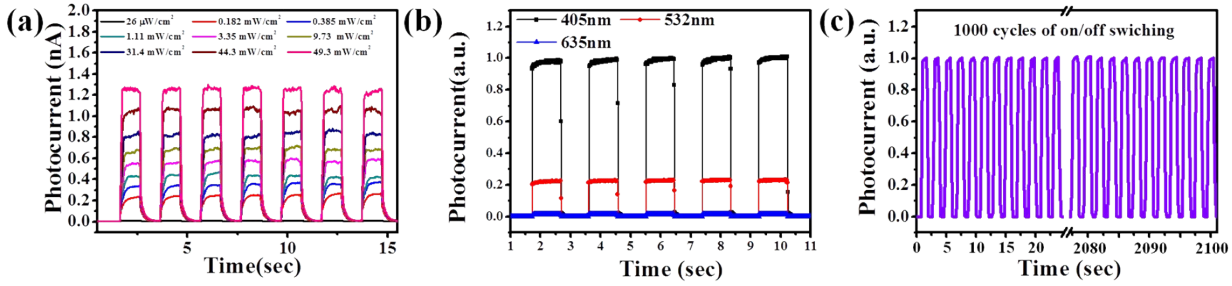

Figure S7. (a) Photoswitching characteristics of the AC-In_2S_3/Si device under various light intensity at V_{ds} = 0 V. (b) Stability and repeatability of the photocurrent under incident light with different wavelengths. (c) Photoresponse of the AC-In_2S_3/Si photodetector in 1000 photoswitching cycles.

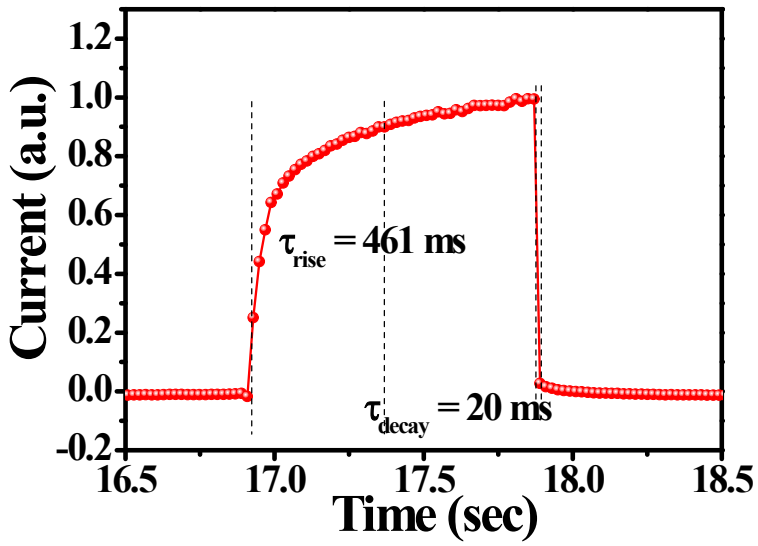

Figure S8. The magnified and normalized plot of one photoswitching cycle of a rectangular-shape In_2S_3 device. The bias voltage is 2 V.

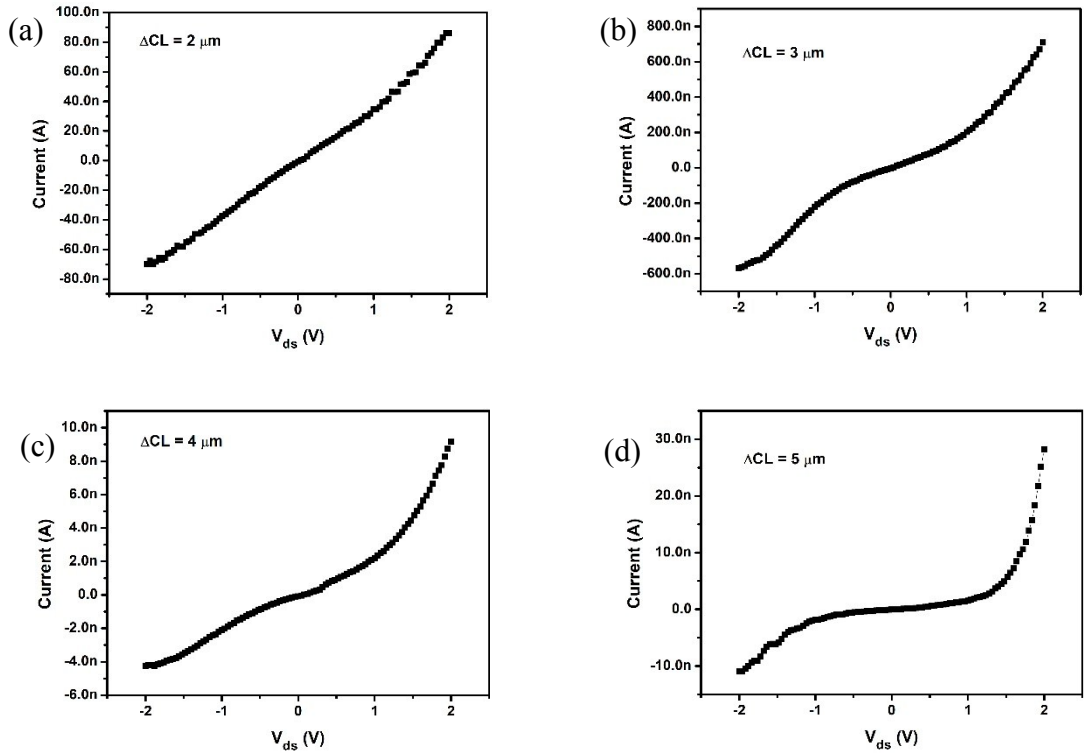

Figure S9. I-V curves of the AC-In_2S_3 photodetectors with various ΔCL: (a) 2 μm; (b) 3 μm; (c) 4 3 μm; (d) 5 μm.

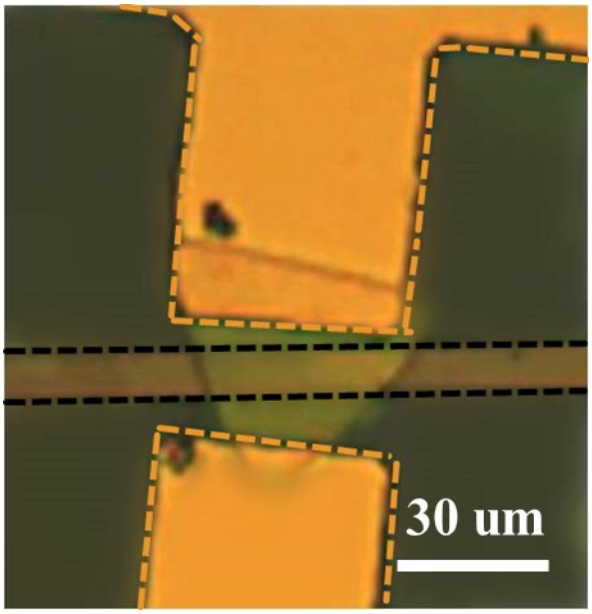

Figure S10. Optical image of the AC-In_2S_3/Si device with Au electrodes.

Table S1. Key parameters of our AC-In_2S_3/Si device and other asymmetric electrode material contact photodetectors.

Devices	Voc (mV)	Rectification ratio	R (mA/W)	D* (Jones)	On/off ratio	Rise/decay time (ms)	Ref.
AC-In_2S_3/Si	**300**	**ND**	**740**	**1.56×10^{10}**	**9×10^4**	**9/10**	**Ours**
AC-In_2S_3	**5**	**2858**	**260**	**6.48×10^9**	**929**	**65/15**	**Ours**
In_2S_3	**ND**	**148**	**ND**	**ND**	**329**	**461/20**	**Ours**
Au/MoS_2/Mo_2C	ND	ND	0.1	ND	ND	23000/28000	5
Au/graphene/Ti	ND	ND	52	ND	ND	ND	6
Au/InSe/In	ND	ND	369	3.35×10^{12}	ND	ND	7
Pt/GaN/Ni	ND	ND	30	1.78×10^{12}	ND	100/100	8
Ag/ZnO/Au	ND	ND	ND	ND	ND	100/100	9
UCNPs/Gr/GaAs	430	ND	5.97	1.1×10^{11}	3.9×10^3	ND	10
Ag/ZnMgO/ZnO	ND	ND	16	5×10^9	ND	2400/3000	11

Ref.: reference. ND: no data. Gr: graphene.

Table S2. Key parameters of our asymmetric AC-In_2S_3/Si device and other asymmetric heterojunction contact photodetectors.

Devices	Voc (mV)	Rectification ratio	R (mA/W)	D* (Jones)	On/off ratio	Rise/decay time (ms)	Ref.
AC-In_2S_3/Si	**300**	**ND**	**740**	**1.56×10^{10}**	**9×10^4**	**9/10**	**Ours**
AC-In_2S_3	**5**	**2858**	**260**	**6.48×10^9**	**929**	**65/15**	**Ours**
In_2S_3	**ND**	**148**	**ND**	**ND**	**329**	**461/20**	**Ours**
Sb-doped ZnO	ND	ND	0.15	9.9×10^8	ND	22000/100	12
MoS_2/WS_2	ND	ND	4.36	4.36×10^{13}	ND	~4	13
CuO/Si	ND	ND	389	3×10^9	ND	0.06/0.08	14
ZnO/CuSCN	37	ND	20	ND	ND	ND	15
NiO/TiO_2	ND	ND	0.065	1.1×10^9	14	1200/7100	16
MoS_2/h-BN/Gr	ND	ND	360	5.9×10^{14}	ND	ND	17

Ref.: reference. ND: no data. Gr: graphene.

Reference

1. McCarthy, R. F.; Schaller, R. D.; Gosztola, D. J.; Wiederrecht, G. P.; Martinson, A. B., Photoexcited carrier dynamics of In_2S_3 thin films. *J. Phys. Chem. Lett.* **2015,** *6* (13), 2554-2561.
2. Ho, C.-H., Growth and characterization of near-band-edge transitions in β-In2S3 single crystals. *J. Cryst. Growth* **2010,** *312* (19), 2718-2723.
3. Li, B.; Huang, L.; Zhong, M. Z.; Li, Y.; Wang, Y.; Li, J. B.; Wei, Z. M., Direct Vapor Phase Growth and Optoelectronic Application of Large Band Offset SnS2/MoS2 Vertical Bilayer Heterostructures with High Lattice Mismatch. *Adv. Electron. Mater.* **2016,** *2* (11), 1600298.
4. Li, Y. T.; Wang, Y.; Huang, L.; Wang, X. T.; Li, X. Y.; Deng, H. X.; Wei, Z. M.; Li, J. B., Anti-Ambipolar Field-Effect Transistors Based On Few-Layer 2D Transition Metal Dichalcogenides. *ACS Appl. Mater. Interfaces* **2016,** *8* (24), 15574-15581.
5. Kang, Z.; Cheng, Y. F.; Zheng, Z.; Cheng, F.; Chen, Z. Y.; Li, L. Y.; Tan, X. Y.; Xiong, L.; Zhai, T. Y.; Gao, Y. H., MoS2-Based Photodetectors Powered by Asymmetric Contact Structure with Large Work Function Difference. *Nano-Micro Letters* **2019,** *11* (1), 12.
6. Yoo, T. J.; Kim, Y. J.; Lee, S. K.; Kang, C. G.; Chang, K. E.; Hwang, H. J.; Revannath, N.; Lee, B. H., Zero-Bias Operation of CVD Graphene Photodetector with Asymmetric Metal Contacts. *ACS Photonics* **2018,** *5* (2), 365-370.
7. Dai, M. J.; Chen, H. Y.; Feng, R.; Feng, W.; Hu, Y. X.; Yang, H. H.; Liu, G. B.; Chen, X. S.; Zhang, J.; Xu, C. Y.; Hu, P. A., A Dual-Band Multilayer InSe Self-Powered Photodetector with High Performance Induced by Surface Plasmon Resonance and Asymmetric Schottky Junction. *Acs Nano* **2018,** *12* (8), 8739-8747.
8. Liu, C. H.; Shi, X. Q.; Liu, Y. D.; Zhang, Y.; Zhai, J. Y.; Wu, W.; Zhang, K.; Peng, M. Z.; Kou, J. Z.; Wang, Z. L., FlexibleSelf-Powered GaN Ultraviolet Photoswitch with Piezo-Phototronic EffectEnhanced On/Off Ratio. *ACS Nano* **2016,** *10* (1), 1572.
9. Lu, S.; Qi, J.; Liu, S.; Zhang, Z.; Wang, Z.; Lin, P.; Liao, Q.; Liang, Q.; Zhang, Y., Piezotronic Interface Engineering on ZnO/Au-Based Schottky Junction for Enhanced Photoresponse of a Flexible Self-Powered UV Detector. *ACS Appl. Mater. Inter.* **2014,** *6* (16), 14116-14122.
10. Wu, J.; Yang, Z.; Qiu, C.; Zhang, Y.; Wu, Z.; Yang, J.; Lu, Y.; Li, J.; Yang, D.; Hao, R.; Li, E.; Yu, G.; Lin, S., Enhanced performance of a graphene/GaAs self-driven near-infrared photodetector with upconversion nanoparticles. *Nanoscale* **2018,** *10* (17), 8023-8030.
11. Fan, M. M.; Liu, K. W.; Chen, X.; Zhang, Z. Z.; Li, B. H.; Shen, D. Z., A self-powered solar-blind ultraviolet photodetector based on a Ag/ZnMgO/ZnO structure with fast response speed. *RSC Advances* **2017,** *7* (22), 13092-13096.
12. Kao, T. H.; Chen, J.-Y.; Chiu, C.-H.; Huang, C.-W.; Wu, W.-W., Opto-electrical properties of Sb-doped p-type ZnO nanowires. *Appl. Phys. Lett.* **2014,** *104* (11), 26.
13. Wu, W. H.; Zhang, Q.; Zhou, X.; Li, L.; Su, J. W.; Wang, F. K.; Zhai, T. Y., Self-powered photovoltaic photodetector established on lateral monolayer MoS2-WS2 heterostructures. *Nano Energy* **2018,** *51*, 45-53.
14. Hong, Q. S.; Cao, Y.; Xu, J.; Lu, H. M.; He, J. H.; Sun, J. L., Self-Powered Ultrafast Broadband Photodetector Based on p-n Heterojunctions of CuO/Si Nanowire Array. *ACS Appl. Mater. Inter.* **2014,** *6* (23), 20887-20894.
15. Garnier, J.; Parize, R.; Appert, E.; Chaix-Pluchery, O.; Kaminski-Cachopo, A.; Consonni, V., Physical Properties of Annealed ZnO Nanowire/CuSCN Heterojunctions for Self-Powered UV Photodetectors. *ACS Appl. Mater. Inter.* **2015,** *7* (10), 5820-5829.
16. Zheng, L.; Feng, T.; Zhang, Z.; Zhao, B.; Fang, X., Large scale, highly efficient and self-powered UV photodetectors enabled by all-solid-state n-TiO2 nanowell/p-NiO mesoporous nanosheet heterojunctions. *J. Mater. Chem. C* **2016,** *4* (42), 10032-10039.

17. Li, H.; Li, X. M.; Park, J. H.; Tao, L.; Kim, K. K.; Lee, Y. H.; Xu, J. B., Restoring the photovoltaic effect in graphene-based van der Waals heterojunctions towards self-powered high-detectivity photodetectors. *Nano Energy* **2019,** *57*, 214-221.